Chapter

Rock Physics Interpretation of Tomographic Solutions for Geothermal Reservoir Properties

Lawrence Hutchings, Brian Bonner, Seth Saltiel, Steve Jarpe and Mariel Nelson

Abstract

We present the basic theory of rock physics, laboratory studies, and field observations that can be applied to interpreting tomographic solutions from microearthquakes for reservoir properties. These properties include location of fluids, fractures, porosity, and permeability. We obtain 3D tomographic solutions for isotropic velocity (*Vp* and *Vs*) and attenuation (*Q p* and *Qs*), and derived solutions for elastic moduli (lambda, bulk and Young's), and Poisson's ratio. We show that a relatively high density of recording stations, about one each km^2, and relatively few microearthquakes (~300) can provide solutions at sufficient resolution and in a relatively short amount of time to be useful for reservoir exploration and management. We provide a case study for The Geysers, California, USA.

Keywords: tomography, reservoir modeling, microearthquakes, rock physics, The Geysers

1. Introduction

Microearthquakes with magnitude (M < ~3) occur naturally or due to fluid injection and production in geothermal, CO_2 sequestration, hydrocarbon, and natural gas reservoirs. In geological environments where sufficient numbers occur, they are a source of energy that provides information about reservoirs not often achieved by other methods. Recordings of microearthquakes can provide 3D tomographic solutions of isotropic velocity (*Vp* and *Vs*) and attenuation quality factors (*Q p* and *Qs*). These results can be used to also obtain solutions for Poisson's ratio, lambda, and Young's and bulk moduli. Furthermore, analysis of the microearthquakes provides locations, moment tensors and stress drops. These results can be combined with basic source theory and rock physics principles to interpret reservoir properties including regions of fluids, fractures, porosity, and permeability. We show that a relatively high density of recording stations, about one each per km^2, and relatively few earthquakes (~300) can provide solutions at sufficient resolution and in a relatively short amount of time to be useful for exploration and reservoir management. We provide a case study for The Geysers, California, USA.

We do not attempt to obtain absolute values from tomography results, as this would require an excessively large number of events. We are interested in anomalies—changes in tomography results for areas with the same statistical resolution, depth, and comparable geology. Anomalies can indicate alterations and possible reservoir conditions. We make extensive use of automation to process the large amount of data collected [1, 2] and a tomographic inversion code designed to work with the output of the automated data processing (SimulCR; [3]).

2. Rock physics

Gassmann [4] first addressed rock physics by defining theoretical rocks based upon fractions of a sample of solid, liquid and gas. Later, more sophisticated approaches (effective medium theories: EMTs) represented rocks by additionally including pore shape (including fractures) and more quantitative descriptions (summarized by Berryman [5, 6]). These theories assume that response of a fractured or porous rock are heterogeneous on a macro-scale, but can be reproduced in a homogeneous rock that is equivalent to the former in the regime of static deformation. These additions better define the relationship among elastic parameters and material properties and therefore how they influence the propagation of seismic waves from microearthquakes. Of course, here and in subsequent discussions, we refer to general results, which sometimes vary.

Rock physics has been used to interpret recordings of active seismic sources primarily for oil and gas studies [6, 7]. Additionally, several authors have previously interpreted microearthquake studies with rock physics [8–14]. The effectiveness of seismic measurements to obtain reservoir properties has been successfully demonstrated for pore fluid pressures in country rock from injected CO_2 [15, 16] and fracture densities in underground repositories [17]. Authors have also used effective medium theory to further interpret tomography [1, 18–20]. Here we attempt to utilize a more comprehensive relationship between microearthquake recordings and material and fluid properties in a geothermal environment. The basic theory of rock physics, laboratory studies, and field observations that can be applied to interpreting tomographic solutions from microearthquakes for geothermal reservoir properties is outlined.

2.1 Seismic velocities

Hooke's Law shows that the strain field resulting from a generalized stress can be separated into a volume change with amplitude λ and a shape change with amplitude μ:

$$s_{ij} = \lambda \epsilon_{ii} \partial_{ij} + 2\mu \epsilon_{ij} \tag{1}$$

where s_{ij} is stress and ϵ_{ii} is strain.

The solution to the wave equation in terms of λ and μ specifies field observables V_p and V_s:

$$\nu_p = \sqrt{\frac{\lambda + 2\mu}{\rho}} = \sqrt{\frac{K + \frac{4}{3}\mu}{\rho}} \tag{2}$$

$$\nu_s = \sqrt{\frac{\mu}{\rho}} \tag{3}$$

where ρ is bulk density of the material and K is bulk modulus (below).

2.2 Elastic parameters

The elastic parameters used in this discussion can be described in terms of seismic velocity and density [7]. These solutions include density. We provide a density value of the aggregate state of the country rock with depth. Density can be removed by division from the solution for shear velocity (Eq. (3)). The parameters are as follows:

Poisson's ratio σ; the ratio of compressional or tensional strain to strain in orthogonal directions.

$$\sigma = \frac{V_p^2 - 2V_s^2}{2\left(V_p^2 - V_s^2\right)}. \tag{4}$$

Poisson's ratio is a valuable tool because it can be calculated from velocities alone and is insensitive to density variations caused by lithology. Seismologists have traditionally used *Vp*/*Vs* and Poisson's ratio interchangeably. However, it is evident that there is not a linear relation between *Vp*/*Vs* and Poisson's ratio, but over the range of values generally observed in seismic data ($0.2 < \sigma < 0.3$) the relationship is essentially linear. Poisson's ratio can range as low as 0.1 for foam, concrete, and dry, gas-saturated sands and as high as 0.5 for a perfectly elastic material, such as rubber at low strain. Cork has a value of 0.0. Effective medium theories (EMT) suggest that Poisson's ratio tends to vary smoothly with rock microstructure and elasticities of porous materials show that different pore shapes produce characteristic values for Poisson's ratio [6].

Shear modulus (μ): the relation of a shear stress to a shear strain in the same direction.

$$\mu = \nu_s^2 \rho. \tag{5}$$

Lambda (λ): the ratio of compressional or tensional stress to strains in orthogonal directions:

$$\lambda = \rho\left(V_p^2 - 2V_s^2\right). \tag{6}$$

Lambda is the off-diagonal component of the isotropic stiffness tensor in the absence of shearing effects and is referred to as incompressibility [5]. It is independent of μ. In the Gassmann model, λ is elastically dependent on fluid properties, while μ is not [5].

Young's modulus (E): the relation between the stress applied and the resulting strain in the same direction:

$$E = \rho V_s^2 \left\{\frac{3R^2 - 4}{R^2 - 1}\right\} \tag{7}$$

with

$$R = \frac{V_p}{V_s} \tag{8}$$

Little research has been done on the relation of Young's modulus to reservoir properties, but we execute an analysis in this study to see if any effects can be identified.

Bulk modulus (K): a measure of how compressible a material is. It relates the volume's change in shape resulting from triaxial or hydrostatic stress:

$$K = V\frac{\partial P}{\partial V} = \rho\left\{V_p^2 - \frac{4V_s^2}{3}\right\}. \quad (9)$$

where V is volume and P is pressure. So, K approaches 0.0 for a fully rigid body. Hereafter lambda, bulk modulus, Young's modulus, and Poisson's ratio are referred to as λ, K, E, and σ, respectively.

2.3 Attenuation

Attenuation is the loss of energy with wave propagation, and Q is the quality quotient that describes the amount of attenuation (Aki and Richards, p. 220). Q has the reciprocal effect of attenuation, i.e., high Q is low attenuation and low Q is high attenuation. Attenuation is generally assumed to be due to inter-crack motion or fluid flow between pores, and is generally called intrinsic attenuation. Extrinsic attenuation is apparent attenuation when seismic energy is scattered due to small fractures. Energy is not actually lost, but a wavefront pulse of a propagating arrival broadens with distance, as would be observed with actual attenuation. Menke [21] fit observations for dry competent rock, and explains how attenuation decreases with depth due to crack closure and stiffening. Tokzoz and Johnson [22] also say this explains why many laboratory studies show attenuation to be frequency independent. In our analysis we do not distinguish pulse broadening due to intrinsic or extrinsic Q. This is determined by comparisons to other attributes. We also assume frequency independent Q.

2.4 Cracks, fractures and faults

Several mechanisms exist for the creation and destruction of permeability at depth; all of these involve cracks, fractures or faults. Cracks are presumed to be associated with weak grain boundaries, fractures are at the scale of multiple cracks, and faults are dislocations from earthquakes. In the most general case, the nucleation and propagation of cracks may increase the connectivity between cracks and fractures, and thus permeability [23]. Fractures alone can be conduits of permeability, as observed in the Salton Sea [19]. Faults are often conduits for fluid flow as well and thus also affect permeability. Faults are considered tectonic in nature and are often aligned with regional stress patterns.

Accurate locations of microearthquakes can often denote permeable zones while their moment tensors can identify the orientation and type of fractures being formed. Guilham et al. [24], Johnson [25] and Julian [26] interpreted moment tensors to obtain focal mechanism solutions that indicate the existence of isotropic and deviatoric dislocation events at The Geysers.

The rupture process and resulting permeability from microearthquakes may not be identical at all scales. Microearthquakes that rupture an entire crack or fracture may have an end effect, i.e., deformation at the end of a fracture to accommodate slip. Johnson [27] theorizes that this gives rise to orthogonal tensile crack opening at the end of cracks or fractures. Microearthquakes associated with faults may rupture only part of a larger feature created by previous earthquakes, thus not create tensile cracks.

Rocks with parallel crack or fracture systems will cause anisotropic wave propagation and shear-wave splitting will occur. In geothermal environments, shear-wave velocity anisotropy has been observed to as high as 10% [28, 29]. Several authors attempt to address anisotropy as a tomography problem in order to identify where it occurs [30, 31]. Rose diagrams [28, 32] only map observed shear-wave splitting and do not identify locations of its occurrence.

Cracks and fractures (C&F) decrease μ without significantly reducing ρ and thus decrease both *Vp* and *Vs*. In the presence of C&F a geologic material is expected to have low *Vp* and *Vs* near the surface due to low μ and generally increase monotonically with depth due to the closure of cracks and fractures as pressure increases from the lithostatic load [33, 34]. Basement rocks at lithostatic pressures consistent with depths of greater than 3 km can be expected to have very low permeability (< 10–3 μ Darcy) due to closure of fractures [35]. At these depths permeability can be due to micro-fractures. Once C&F close, velocity will no longer increase with depth. O'Connell and Budiansky [36] relate a C&F density parameter to the effective Poisson's ratio, which is a direct reflection of their effect on *Vp* and *Vs*. λ, *B*, and *E* will also increase with depth due to compliance from open C&F.

In hydrothermal environments, grain-scale geochemical reactions can cement micro-fractures and stiffen the rock matrix. As a result, their relative effect on velocity will be reduced. This is observed in laboratory measurements of velocities in recovered core from The Geysers [33]. This suggests that much of the observed depth dependence of *Vp* and *Vs* in The Geysers reservoir rocks is due to closure of larger-scale C&F. Large permeable fractures might then be identified by regions of high velocity gradients in field data with a high density of compliant fractures. This may be particularly true in geothermal areas where healed micro-fractures will contribute less to observed gradients [33, 37].

Attenuation is also significantly affected by C&F. C&F increase extrinsic attenuation and reduce *Qp* and *Qs*. The lithostatic load tends to decrease extrinsic attenuation with depth due to closure of C&F. Extrinsic attenuation is potentially different for *P*-wave propagation and thus *Qp* than for *S*-wave propagation and *Qs* if C&F are aligned, since particle motion is transverse.

2.5 Effects of fluids and steam

Following Eqs. (2) and (3), the inclusion of fluids into either pores or fractured material increases density and decreases *Vp* and *Vs*. Fluids also increase the bulk modulus, which increases *Vp*. In low porosity rocks, increased bulk modulus generally dominates the increase in density, whereas the reverse is true for high porosity rocks. The shear modulus (μ) is independent of fluids in the absence of geochemical effects and is determined by the porous rock matrix [6]. Therefore, density changes are the only effect that fluids have on *Vs*.

Injection of fluids can cause micro-fractures and/or microearthquakes due to thermal contraction or hydro-fracturing. Fluids also significantly affect attenuation. Partial saturation increases intrinsic attenuation. However, full saturation should lower intrinsic attenuation by inhibiting diffusion. Diffusion is also different for *P*-wave propagation and thus *Qp* than for *S*-wave propagation and *Qs* because particle motion is transverse. We note that *Qs* decreases and *Qp* increases with saturation (**Figures 5** and **6**).

Berryman et al. [8] emphasized that lambda and density contain information about saturation, while both combined with shear modulus contain information about porosity. Berryman et al. recast λ (Eq. (6)) as λ/μ, removing density $\left(\rho = \mu/v_s^2\right)$ and showing lambda's application in identifying the degree of saturation and type of saturation, i.e., the arrangement of fluids in a rock (inhomogeneous or homogeneous). They showed that for homogeneous saturation, λ/μ remains low for partial saturation and high for full saturation, and for inhomogeneous saturation there is a monotonic increase in λ/μ as saturation increases (equal at full saturation).

Typically, seismologists use high values of Poisson's ratio (or *Vp/Vs*) to indicate fluid saturation. There is a dramatic increase in Poisson's ratio with saturation by

the replacement of vapor by water, which increases the effective bulk modulus, while *Vs* is unaffected by fluid content.

Laboratory work suggests that using a combination of attenuation and velocity can improve discrimination of pore fluid content. Winkler and Nur [38] measured moduli and attenuation for longitudinal and torsional modes in porous and cracked rock near 1 kHz, where intrinsic attenuation dominates extrinsic attenuation. Plotting the data in Q_p/Q_s and V_p/V_s coordinates separates dry, partially saturated, and fully saturated conditions. These data cannot be used quantitatively until more measurements are done with low frequency data. The strong trends in Winkler and Nur's data suggest, however, that field data should reflect similar effects. Thus, values above a slope of 1.0 for Q_p/Q_s versus V_p/V_s plot indicate saturation and lower values indicate drier conditions. Hutchings et al. [3] found that The Geysers' data supported Winkler and Nur's theory.

Gritto [39] theorized that when injected water contacts reservoir rock, heat is drawn from the reservoir rock until the water vaporizes. The resulting cooling and contraction of the rock generates tensile (mode I) cracks and subsequent micro-seismicity. Once all water is converted to steam, the rock remains at a stable temperature with no further seismicity and the reservoir has reached maximum steam concentration. Permeability can be measured by monitoring the spatial and temporal migration of the micro-seismic cloud associated with fluid injection [40]. The resulting cooling may also result in increased shear moduli.

2.6 Temperature and pressure effects

Rocks subjected to high temperatures and pressures undergo a transition from brittle to crystalline plastic behavior. The temperature of this transition ranges from around 300°C (quartz) to 400–450°C (feldspar) and also depends on pressure and strain rate [41, 42]. When stressed, some rocks may undergo cataclastic flow, which is characterized by ductile stress-strain behavior as well as cracking and frictional sliding.

The effect of temperature can oppose the effect of pressure [34]. In a dynamic situation, heating or cooling of fluids within pores can cause fractures and increase permeability while pressure can close fractures. Experiments where granite was cooled from high temperatures up to 646°C showed permeability increased up to a 1000 times over original values [43]. Darot et al. also found permeability decreased rapidly with confining pressure, being effectively zero for confining pressures over 30 MPa.

2.7 Summary: porosity, permeability, and saturation

There are seven primary interpretations of porosity, permeability and saturation from observable microearthquake data. Comparisons are made relative to normal geology at similar depths and temperatures, meaning geology that has a monotonic increase in velocity and Q as a function of depth, and saturation, porosity and temperature that is considered average for the geologic condition of the study area. The interpretations are as follows:

1. *Dry competent geology with low porosity* might be identified by increased *Vp* and *Vs* due to high shear modulus due to few C&F; high Q_p and Q_s due to lack of diffusion and little extrinsic attenuation due to few C&F; Poisson's ratio near 0.25; lambda, bulk and Young's modulus are relatively high due to incompressibility of stiff material. No fracturing or permeability is assumed.

2. *Dry competent geology with high porosity* might be identified by a slight increase in *Vs* due to lower density, and a decrease or no change is *Vp* due to low bulk modulus offsetting low density with *Q*$_p$ and *Qs* relatively unchanged. Poisson's ratio is slightly decreased due to higher Vs and lower Vp. Young's modulus and lambda are relatively low due to compressibility and dry conditions. No fracturing or permeability is assumed.

3. *Dry fractured geology* might be identified by lower *Q*$_p$ and *Qs* due to an increase in extrinsic attenuation and lower *Vp* and *Vs* due to a decrease in shear modulus. Poison's ratio, bulk modulus, Young's modulus and lambda are decreased due to increased compressibility. No permeability is assumed, and conditions are the same if the material is high or low porosity.

4. *Saturated competent geology with low porosity* might be identified by slightly higher *Q*$_p$ due to reduced intrinsic attenuation and *Qs* may be low due to saturation. A small decrease in *Vs* is expected due to an increase in density with slightly higher or unaltered *Vp* due to an increase in bulk modulus (possibly offset by increased density). Poisson's ratio and lambda will be higher, shear modulus unchanged, and Young's modulus slightly higher due to decreased compressibility. Partial saturation reduces these effects.

5. *Saturated competent geology with high porosity* might be identified by slightly higher *Q*$_p$ due to reduced intrinsic attenuation and *Qs* may be low due to saturation. A significant decrease in Vs is expected due to an increase in density and little change or increase in *Vp* due to an increase in density and a counter-effect of increased bulk modulus. Poisson's ratio and lambda will be significantly higher with shear modulus unchanged. Young's modulus will be higher. Permeability might be assumed. Partial saturation reduces these effects.

6. *Saturated fractured geology with high porosity* might be identified by significantly lower *Q*$_p$ and *Qs* due to an increase in both extrinsic and intrinsic attenuation; a significant decrease in *Vs* due to an increase in density and a reduction of the shear modulus due to fractures; and an increase in *Vp* due to the dominating effect of high bulk modulus (or lambda). The increase in density and decrease in shear modulus have a mitigating effect. Permeability is likely high due to intersecting and open fractures. Poisson's ratio is high. Bulk modulus, Young's modulus, and lambda will be higher due to saturation and incompressibility.

7. *Saturated fractured geology with low porosity* might be identified by lower *Q*$_p$ and *Qs* due to an increase in extrinsic, but little increase in intrinsic *Q*. Moderately low *Vs* is expected due to a decrease in shear modulus with little increase in density and lower or unaltered *Vp* is expected due to the competing effects of decreased shear modulus and increased bulk modulus. Permeability is likely high due to intersecting and significantly open fractures. Poisson's ratio is unchanged or moderately higher. Young's modulus and lambda are significantly higher due to saturation.

3. Case study: the Geysers

Hutchings et al. [3] analyzed a ~5.5 km^3 volume at the Northwest Geysers area (**Figure 1a**). Seven injection wells were in operation in this volume during the

period of the study (**Figure 1b**). The known locations of induced events, the timing, rate, and location of water injection, and the location of geologic alterations at the bottom of injection wells provide a test of tomography and a rock physics approach to reservoir property analysis. The study is divided into two time periods, approximately 42 days before and 31 days after injection rates changed significantly at several of the wells. **Figure 1** shows microearthquake locations, recording station locations, and wells utilized in the study.

The study area is within a portion of The Geysers geothermal field that has a high temperature reservoir (HTR, with temperatures up to 400°C) that underlies a normal temperature reservoir (NTR, with temperatures about 260°C) shown in **Figure 2** [44]. The HTR extends downward from about ~2 km below mean sea level (bmsl) in the southwest to ~3 km bmsl in the northeast. The NTR reservoir extends between ~1.5 and ~2 km bmsl [44]. The rocks are composed of relatively permeable greywacke in the NTR and of low-permeability, thermally altered greywacke in the HTR.

We separated data into two recording time periods and performed tomography, the first from 1 September to 8 October 2011 and the second from 9 October to 11 November 2011. We refer to these as period 1 and period 2 in the text. Tomography was performed with 23 recording stations, about one station per 1.3 km^2, and with 378 and 369 earthquakes for the two time periods. The first time period is for 42 days before and the second is for 31 days after injection rates changed significantly at several of the wells.

Figures 3 and **4** show *Vs* and *Vp* tomography results for a cross section that passes through the bottom of wells WH34 and Prati-32 along with a cross section that passes through the bottom of wells Prati-9 and Prati-54. These are shown as AA′ and BB′ in **Figure 1**. Also shown is the resolution value for diagonal of the resolution matrix for the tomography. **Figure 3a** shows the thickening of the Greywacke seen in **Figure 2**. There is very little change in the *Vp* tomography

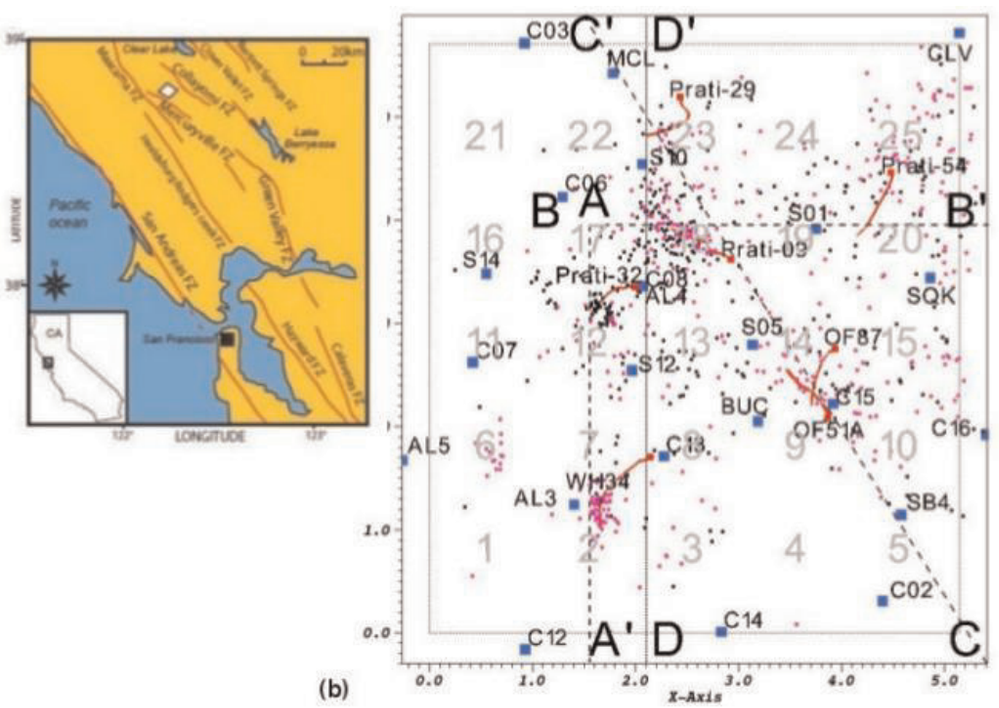

Figure 1.
(a) Regional setting and the location of the study area (white diamond) and locations of major faults. (b) Map view of study area—recording stations in blue squares, earthquakes from first period in magenta dots and those during the second period in black dots, wells in red (red square is top of well), and the cross section locations AA′, BB′, CC′, and DD′ discussed in text. The study area is rotated 39° clockwise, so CC′ is aligned almost due north.

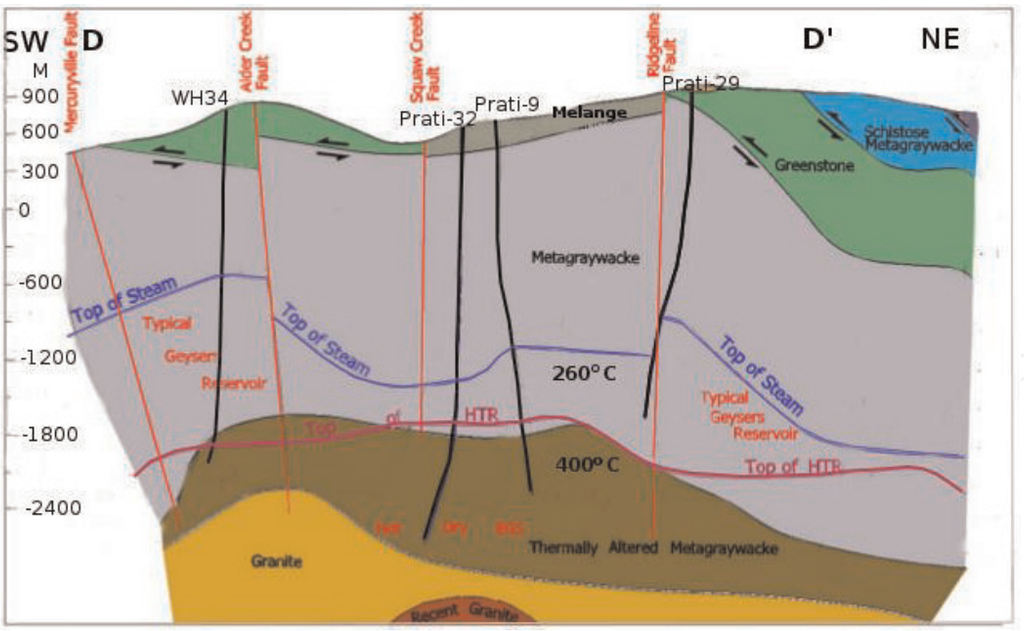

Figure 2.
Geologic cross section along DD′ in ***Figure 1b****, view is northwest; modified from [44].*

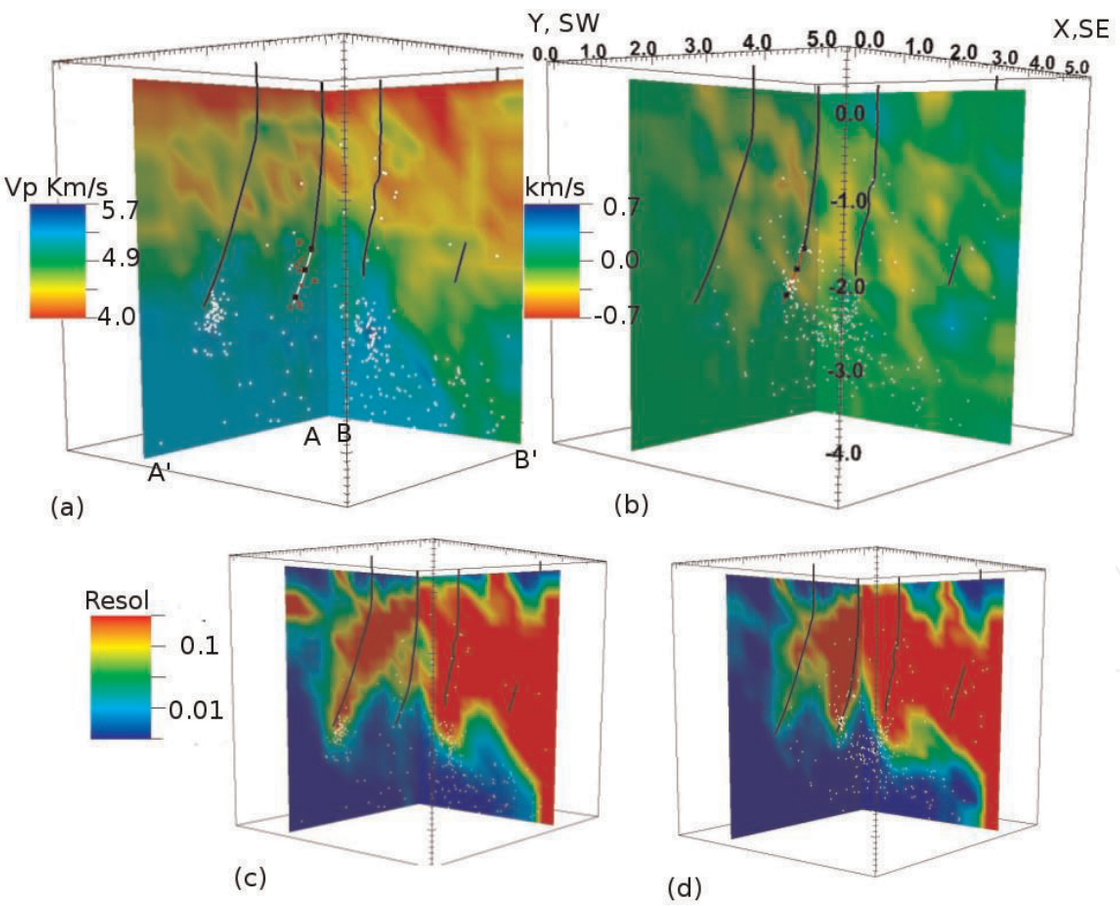

Figure 3.
(a) Vp tomography results for period 1 along cross sections AA′ and BB′ shown in ***Figure 1b****; (b) changes in Vp results for period 2, i.e., ΔVp; (c) resolution for period 1; (d) resolution for period 2.*

results for the second time period. The red dots at the bottom of Prati-32 are location of the first events that occurred after injection started (located with the tomography results from the first time period). The black squares are the steam entry points. That the first few events occur near the wells and near the

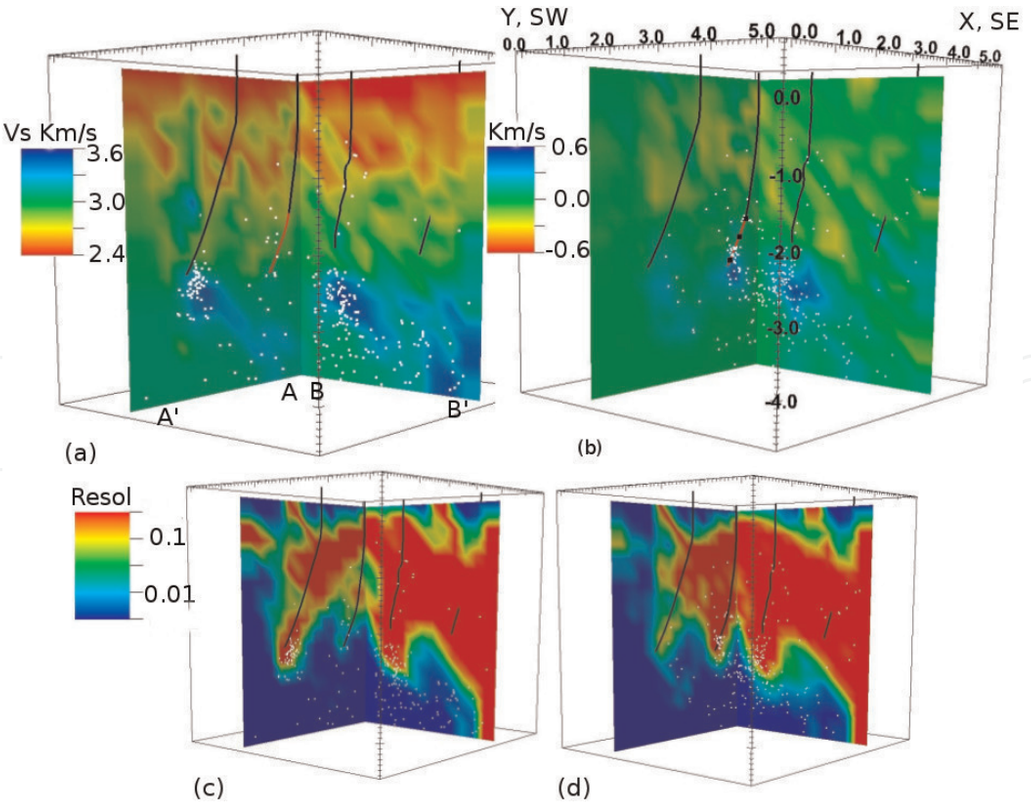

Figure 4.
(a) Vs tomography results for period 1 along cross sections AA′ and BB′ shown in ***Figure 1b****; (b) changes in Vs results for period 2, i.e., ΔVs; (c) resolution for period 1; (d) resolution for period 2.*

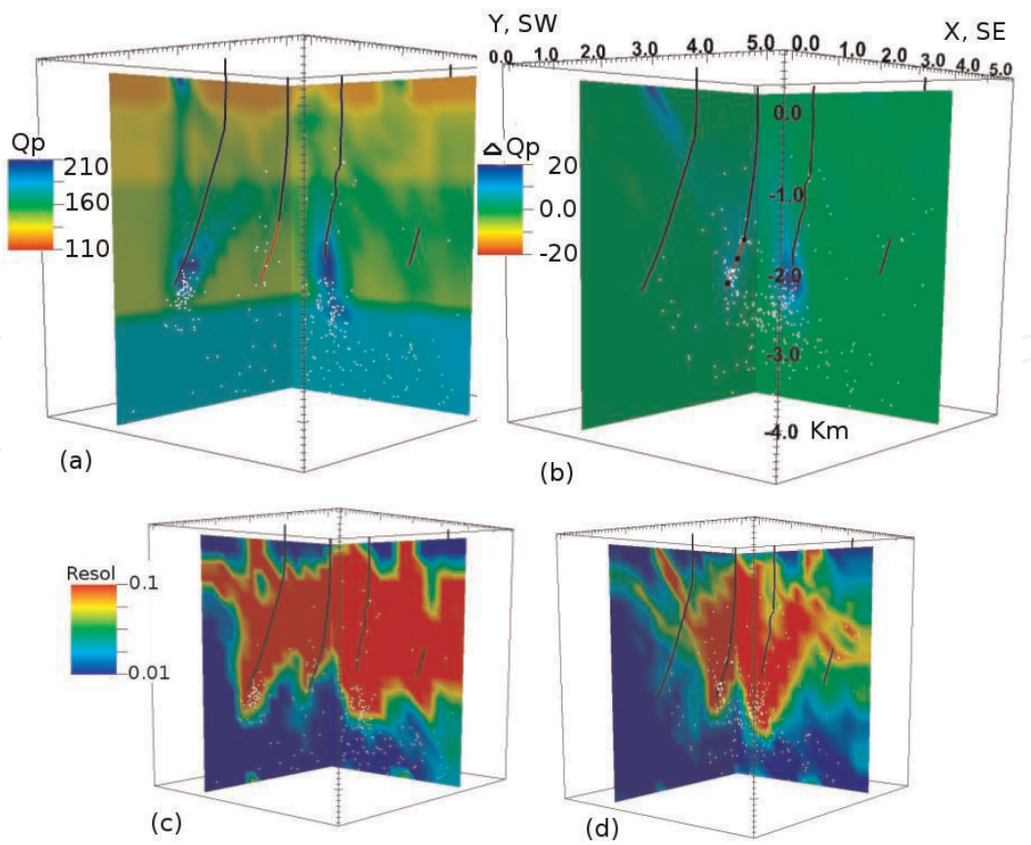

Figure 5.
(a) Q p tomography results for period 1 along cross sections AA' and BB' shown in ***Figure 1b****; (b) results for ΔQ p for period 2, Q p scale on left; (c) resolution for period 1; (d) resolution for period 2. Resolution scale is for diagonal of resolution matrix, where red is greater than 0.1 and blue is less than 0.01.*

steam entry points (and presumably the water release points) and validates the accuracy of the earthquake locations, and subsequently the tomography results.

From **Figure 4a**, there are relatively high *Vs* anomalies below WH34, Prati-9 and possibly Prati-54 (extreme lower right) with no anomaly below Prati-32. These anomalies indicate about a 20% increase in *Vs*. **Figure 4b** shows the change in tomography results for *Vs* during period 2. The anomaly below Prati-9 shows a further increase in *Vs* and a new anomaly appeared below Prati-32. The anomalies below WH34 and Prati-54 have remained unchanged. The high velocity anomalies below WH34, Prati-32 and Prati-9 extend from the bottom of the wells and are not randomly occurring; we conclude they are not artifacts. Seismicity is distributed around the wells and throughout the deeper portions of the volume (>−1.0 km). The resolution in the anomalous areas below the wells is in the range we consider acceptable for our purposes. The new anomaly below Prati-32 during period 2 demonstrates that temporal changes in reservoir properties can be observed over at least a month.

Figures 5 and **6** show Q_p and Q_s tomography results for the same cross sections as for **Figures 3** and **4**. The value for the diagonal of the resolution matrix is also shown. **Figures 5b** and **6b** show the changes in Q_p and Q_s for the second time period, respectively. It is apparent from comparing the background Q values obtained in the inversion for the two time periods that the tomography has only significantly changed around the well bottoms. We conclude that the anomalies at the bottom of wells WH34 and Prati-9 are significant. Q_p increased and Q_s diminished considerably. The Q anomalies envelop the base of the wells and are not

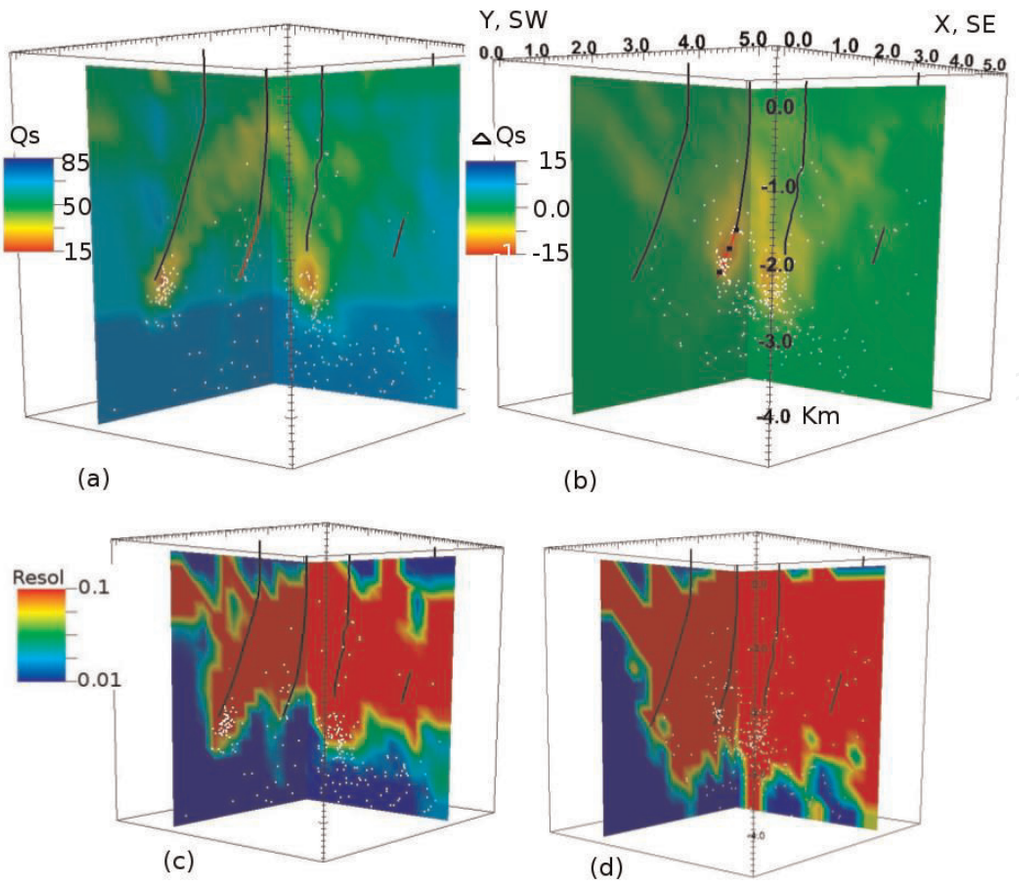

Figure 6.
(a) Qs tomography results for period 1 along cross sections AA' and BB' shown in ***Figure 1b****; (b) results for ΔQs for period 2, Qs scale on left; (c) resolution for period 1; (d) resolution for period 2. Resolution scale is for diagonal of resolution matrix, where red is greater than 0.1 and blue is less than 0.01.*

located exactly where the *Vp* and *Vs* anomalies are observed. No other anomalies are apparent in the results. The anomaly at the bottom of Prati-9 increased in size and the anomaly below WH34 remained unchanged. The background values remained unchanged for the two time periods, so we are fairly confident the anomalies are real and the change below Prati-9 is real.

3.1 Interpretation

Our primary interpretation is that the anomalies we observe are the result of cold water injected into hot material. The wells below which no alteration was observed, and no earthquakes, were Prati-29, Prati-54, OF87A, OF51A and Prati-54. These are located at shallower depths and at cooler temperatures than wells WH34, Prati-32, and Prati-9, where alterations were observed and which are within the hot deep zone. Possible alterations below Prati-54 and OF51A exist at depths far enough below the wells to be located in the hot zone. These observations support our hypothesis that the alterations we observe are a result of cold water injected into very hot geology, which also causes earthquakes. Further, injected water has percolated down to very hot geology. Thus, water responding to gravity reaches as deep as 1.5 km below the wells (and possibly 4.5 km below Prati-54), causing the anomalies.

We further hypothesize that injection cools rock near the well bottoms, which stays cool and saturated as injection continues. Cooling near the well bottoms generates tensile cracks and subsequently micro-seismicity. As water turns to steam, a pressure front triggers more earthquakes away from the wells. However, there is not a concentration of seismicity in the high *Vs* anomalies, but throughout the deep zone, suggesting that the hot deep geology is not ductile enough to be aseismic.

In addition to shear modulus, lambda also decreases (not shown), offsetting the increase in shear modulus so the change in *Vp* is not pronounced. Density does not increase because the fluid turns to steam. Poisson's ratio gets extremely low (not shown), mostly due to the significant increase in *Vs* with little change in *Vp*. Young's modulus is high and bulk modulus is low (not shown), which we interpret as pores filled with steam, but in other portions of the surrounding deep zone, Young's modulus is high and bulk modulus is normal, which we attribute to normal rock properties. In Eq. (6), lambda decreases in value by $-Vs^2$, so a low value of lambda is not surprising. In Eq. (9), bulk modulus is similarly reduced by a factor proportional to $-Vs^2$. In Eqs. (7) and (8), Young's modulus is proportional to $+Vs^2$, so its increase is also not surprising.

There are high Qp and low *Qs* anomalies at the bottom of wells WH34, Prati-32 and Prati-9. The cold water in hot material causes fracturing and a significant increase in seismicity in addition to saturation (initially, before the water turns to steam). If a region is partially saturated, one would expect both intrinsic and extrinsic *Q* to be low, which could account for the low *Qs* anomaly. But the high Qp anomaly poses several issues. If material is fully saturated, intrinsic *Q* would be high, as there would be no movement between pores. However, *Qs* would still reflect the fractures because *Vs* is relatively unchanged by the presence of water. Qp might be high due to high intrinsic Q and high bulk modulus, so perhaps fractures are not reflected in Qp, meaning extrinsic Qp would also be high. Furthermore, the particle motion of shear waves is orthogonal to the compressional motion of the *P*-waves, alignment of fractures may also have an effect. Fractures parallel to *P*-wave particle motion would not alter *Q* and fractures perpendicular to shear-wave particle motion perpendicular to fractures would alter Qp. Since our

tomography does not differentiate between the geometry of attenuation types, we cannot say for sure which is occurring. There are some studies that support the difference between Qp and Qs under saturation conditions.

Tokzoz et al. [45] and Johnston and Tokzoz [46] both show that under dry conditions $Qp \sim Qs$, but under full saturation $Qs < Qp$, agreeing with our observations. This occurs under pressure but at ultrasonic frequencies. DeVilbiss-Munoz [47] shows that Qp and Qs increases significantly as water turns to steam and Mavkov and Nur [48] show Qs increases relative to Qp as saturation increases. Neither of these are consistent with our interpretation.

3.2 Reservoir analysis

We examine observations of normal temperature reservoir depths in the greywacke, from ~1 to 2.5 km bmsl. The top of the steam/liquid boundary is at about 1 km bmsl and deepens to the southeast (**Figure 2**). Lowenstern and Janik [49] point out that the northwest portion of The Geysers has little condensed liquid and contains primarily steam-filled pores. Wells Prati-29 and OF87A-11 are shallower than the other wells in this study and were drilled into the greywacke. OF51A-11 and Prati-54 are deeper, but are located in the eastern portion of the field where the greywacke deepens, so their temperature is comparable to the shallower wells and is included in this discussion. Interestingly, no anomalies in our eight attributes are observed at the bottom of these wells. Temperatures are near 240°C and are apparently too low to induce the effects seen at the other wells drilled into the thermally altered greywacke with temperatures near 400°C or higher.

To identify anomalies at reservoir depths, we used the tomography results for the second time period, which used the results from the first time period as a starting model. Results in the depth range of interest here did not change significantly for the second time period (**Figures 3–6**). We examined values of the eight parameters for voxels that are 1 × 1 km laterally and 0.75 km in depth throughout the study volume. Each voxel is identified by whether the of majority of the volume visually shows high, low or no anomaly. Values are relative to what would be expected for normal geology at comparable depth and resolution. These observations are put into rows of **Table 1**, where one row is for each voxel; there are fifty rows for our approximately 5 × 5 km study area.

Figure 1 shows the surface projection of the location of the volumes, two volumes for each ID number. The ID numbers are listed in the first row of **Table 1**. The second column identifies the center of the voxel in kilometers relative to the origin for X and Y. Regarding the eight attributes, "0" indicates no anomaly, "+" a positive and "–" a negative anomaly. Generally, an anomaly is identified as being at least plus or minus 20% of average values at the same depth and geology. The final column provides a rock physics interpretation based on the eight conditions described in the introduction, which are derived from the basic principles outlined in Section 2. Zero change across the row indicates standard reservoir conditions, which is likely greywacke with steam-filled pores. It is assumed that there is not strict compliance with the eight descriptions in Section 2.8—for example, a voxel with a "0" value in the table may still show a slight change.

The anomalies identified in **Table 1** can be seen in some of the cross sections. **Figure 1** cross section CC′ is aligned almost north-south, so cross section AA′ represents the western portion and BB′ represents the eastern portion of the study volume; the upper part of CC′ represents the northern part and the bottom part of CC′ represents the southern part through the middle of the study area.

ID	*X*, *Y*	*Vp*	*Vs*	*Q p*	*Qs*	Poiss. ratio	Lam.	Bulk	Young's	Interpretation
1	0.6, 0.7	0	0	0	0	0	0	0	0	Standard reservoir
		0	0	0	0	0	+	+	0	(4) Saturated competent geology with low porosity
2	1.6, 0.7	0	0	0	0	0	0	0	0	Standard reservoir
		0	0	0	0	+	+	+	0	(4) Saturated competent geology with low porosity
3	2.6, 0.7	–	0	0	0	0	–	0	0	(2) Dry competent geology with high porosity
		0	0	0	0	0	0	+	0	Standard reservoir
4	3.6, 0.7	0	0	0	0	0	0	0	0	Standard reservoir
		0	0	0	0	0	0	0	0	Standard reservoir
5	4.6, 0.7	0	0	0	0	0	0	0	0	Standard reservoir
		0	0	0	0	0	0	0	0	Standard reservoir
6	0.6, 1.7	0	0	0	0	0	0	0	0	Standard reservoir
		0	0	0	0	0	0	+	0	Standard reservoir
7	1.6, 1.7	0	+	0	+	0	0	0	0	(1) Dry competent geology with low porosity
		0	0	+	0	0	+	+	0	(4) Saturated competent geology with low porosity
8	2.6, 1.7	0	0	0	0	0	–	0	0	Standard reservoir
		0	0	0	0	0	0	0	0	Standard reservoir
9	3.6, 1.7	0	0	0	0	0	0	0	0	Standard reservoir
		0	0	0	0	0	0	+	0	Standard reservoir
10	4.6, 1.7	0	0	0	0	0	–	0	0	Standard reservoir
		0	0	0	0	0	–	0	0	Standard reservoir
11	0.6, 2.7	0	0	0	0	0	0	0	0	Standard reservoir
		0	0	0	0	0	+	+	0	(4) Saturated competent geology with low porosity
12	1.6, 2.7	0	0	+	0	0	0	0	0	Standard reservoir
		0	0	0	0	0	0	0	0	Standard reservoir
13	2.6, 2.7	0	0	0	0	0	0	0	0	Standard reservoir
		0	0	0	0	0	0	0	0	Standard reservoir
14	3.6, 2.7	0	0	0	0	0	–	0	0	Standard reservoir
		0	0	0	0	0	0	0	0	Standard reservoir
15	4.6, 2.7	–	0	0	0	0	0	0	0	Standard reservoir
		0	0	0	0	0	–	0	0	Standard reservoir
16	0.6, 3.7	0	0	0	0	0	0	0	0	Standard reservoir
		0	0	0	0	0	+	+	0	(4) Saturated competent geology with low porosity
17	1.6, 3.7	0	0	0	0	0	0	0	0	Standard reservoir
		0	0	0	0	0	+	+	0	(4) Saturated competent geology with low porosity

ID	*X*, *Y*	*Vp*	*Vs*	*Q p*	*Qs*	Poiss. ratio	Lam.	Bulk	Young's	Interpretation
18	2.6, 3.7	0	0	+	0	0	0	0	0	Standard reservoir
		+	0	+	–	+	+	+	0	(5) Saturated competent geology with high porosity
19	3.6, 3.7	–	0	0	0	–	–	0	0	(2) Dry competent geology with high porosity
		0	0	0	0	0	0	0	0	Standard reservoir
20	4.6, 3.7	0	0	0	0	0	0	0	0	Standard reservoir
		0	0	0	0	0	–	0	0	Standard reservoir
21	0.6, 4.7	0	0	0	0	0	0	0	0	Standard reservoir
		0	0	0	0	0	+	+	0	(4) Saturated competent geology with low porosity
22	1.6, 4.7	0	0	0	0	0	0	0	0	Standard reservoir
		0	0	0	0	0	+	+	0	(4) Saturated competent geology with low porosity
23	2.6, 4.7	0	0	0	0	0	0	0	0	Standard reservoir
		+	0	0	0	0	+	+	0	(4) Saturated competent geology with low porosity
24	3.6, 4.7	–	0	0	0	0	–	0	0	(2) Dry competent geology with high porosity
		0	0	0	0	0	–	0	0	Standard reservoir
25	4.6, 4.7	–	0	0	0	–	–	0	0	(2) Dry competent geology with high porosity
		0	0	0	0	–	–	0	0	(2) Dry competent geology with high porosity

Table 1.
Location of quadrants where tomography attributes are examined.

4. Discussion and conclusions

We analyze eight attributes tomographic images obtained from tomographic images: isotropic velocity (*Vp* and *Vs*), attenuation (*Q p* and *Qs*), and derived elastic moduli (lambda, bulk and Young's) and Poisson's ratio, in addition to earthquake locations. The known locations of induced events, the timing, rate, and location of water injection, and the location of geologic alterations at the bottom of injection wells provide a test of this rock physics approach to reservoir property analysis. We outline rock physics principles that can be used to interpret reservoir properties from these observations. We demonstrate that using a relatively high density of stations and examining anomalies, we obtain results in a shorter time period, with higher accuracy, and with fewer earthquakes than is typical for reservoir studies. We also apply a systematic rock physics evaluation of 50 1 km^3 volumes at reservoir depths and demonstrate the ability to identify reservoir properties. In the deeper portion of the volume (near the well bases, below the existing reservoir), seven of the eight attributes show significant effects of cold water injected into hot material and variations over a two-month time span. The results also suggest water is penetrating as deep as 1.5 km and possibly 4.5 km below the wells, even though temperatures reach at least 400°C in the country rock. This causes an increase in shear

modulus due to cooling, however, due to the temperature, the water quickly turns to steam.

We consider explanations for the relatively high *Vs* estimates in the hot deep zone exhibited in **Figure 3**. Noted earlier, these anomalous regions occur at depths comparable to or deeper than the well termination depths within the HTR (**Figure 2**). This is where the natural reservoir temperatures increase from a relatively homogenous 240°C in the NTR (~900–1800 m bmsl) to at least 400°C, measured at the base of Prati-32 (2672 m bmsl), the deepest wellbore [44]. The pockets of high *Vs* observed in period 1 appear to spatially correspond with wells where water was actively being injected. Furthermore, during period 2, these anomalies intensified only below well bores in which the injection rate increased substantially relative to period 1 (Prati-32, Prati-9, **Figure 3**), including the unambiguous appearance of a new anomaly below Prati-32 associated with the injection of water into a previously undisturbed region of the HTR. The enhanced geothermal system (EGS) demonstration at Prati-32 is therefore an exemplary scenario for considering likely mechanisms to account for the observed evolution of higher *Vs* zones in the HTR, requiring changes in the physical properties of the reservoir material in the range of 30% decrease in bulk density or a 45% increase in shear modulus.

Author details

Lawrence Hutchings[1*], Brian Bonner[1], Seth Saltiel[2,3], Steve Jarpe[4] and Mariel Nelson[2]

1 Lawrence Berkeley National Laboratory, California, United States

2 Department of Earth and Planetary Sciences, University of California, Berkeley, United States

3 Department of Geophysics, University of Chile, Santiago, Chile

4 Jarpe Data Solutions, Inc., Berkeley, California, United States

*Address all correspondence to: ljhutchings@lbl.gov

References

[1] Hutchings L, Bonner B, Jarpe S, Singh A. Microearthquake Analysis for reservoir properties at the Prati-32 injection test, The Geysers, California. In: Proceedings, Geothermal Resources Council, Las Vegas, Nevada. 2014

[2] Hutchings L, Jarpe S, Boyle K, Viegas G, Majer E. Inexpensive, Automated Microearthquake Data Collection and Processing System for Rapid, High-Resolution Reservoir Analysis. Geothermal Resources Council, Transactions. In: 2011 Annual Meeting; San Diego, CA. 2011

[3] Hutchings L, Bonner B, Jarpe S, Singh A. Micro-earthquake analysis for reservoir properties at the Prati-32 injection test, The Geysers, California. In: Proceedings, Geothermal Resources Council; Portland: Oregon; 2014;**38**: 519-526

[4] Gassmann F. Translated, Berryman, "Origin of Gassmann's equation". Geophysics. 1951;**64**:1627-1629

[5] Berryman JG. Mixture theories for rock properties. In: Ahrens TJ, editor. Rock Physics & Phase Relations, a Handbook of Physical Constants, AGU Reference Shelf 3. Washington, DC: American Geophysical Union; 1995. pp. 205-228

[6] Berryman JG. Seismic waves in rocks with fluids and fractures. Geophysical Journal International. 2007;**171**:954-974

[7] Mavko G, Mukerji T, Dvorkin J. The Rock Physics Handbook: Tools for Seismic Analysis of Porous Media. Cambridge: University; 2009

[8] Berryman JG, Berge PA, Bonner BP. Estimating rock porosity and fluid saturation using only seismic velocities. Geophysics. 2002;**67**(2):391-404

[9] De Siena L, Del Pezzo E, Bianco F. Seismic attenuation imaging of Campi Flegrei: Evidence of gas reservoirs, hydrothermal basins, and feeding systems. Journal of Geophysical Research. 2010;**115**:B09312. DOI: 10.1029/2009JB006938

[10] Foulger GR, Julian BR, Pitt AM, Hill DP, Malin P, Shalev E. Tomographic crustal structure of Long Valley caldera, California, and evidence for the migration of CO_2 between 1989 and 1997. Journal of Geophysical Research. 2003;**5**:995-1022

[11] Foulger GR, Grant CC, Ross A, Julian BR. Industrially induced changes in earth structure at the geysers geothermal area, California. GRL. 1997; **24**(2):135-137

[12] Grechka V, Mazumdar P, Shapiro SA. Predicting permeability and gas production of hydraulically fractured tight sands from microseismic data. Geophysics. 2010;**75**(1):B1-B10

[13] Hatchell P, Bourne S. Strain-induced time-lapse time shifts are observed for depleting reservoirs. The Leading Edge. 2005;**24**(12):1222-1225

[14] Julian BR, Ross A, Foulger GR, Evans JR. Three-dimensional seismic image of a geothermal reservoir: The geysers, California. Geophysical Research Letters. 1996;**23**:685-688

[15] Gritto R, Daley TM, Myer LR. Joint cross-well and single well seismic studies of CO_2 injection in an oil reservoir. Geophysical Prospecting. 2004;**52**:323-339

[16] Daley TM, Schoenberg MA, Rutqvist J, Nihei KT. Fractured reservoirs: An analysis of coupled elastodynamic and permeability changes

from propressure variationion. Geophysics. 2006;**71**:033-041

[17] Gritto R, Korneev VA, Daley TM, Feighner MA, Majer EL, Peterson JE. Surface-to-tunnel seismic tomography studies at Yucca Mountain, Nevada. Journal of Geophysical Research. 2004; **109**(B3):B03310. DOI: 10.1029/ 2002JB002036 LBNL-50470

[18] Berge P, Hutchings L, Wagoner J, Kasameyer P. Rock Physics Interpretation of P-Wave Q and Velocity Structure, Geology, Fluids and Fractures at the Southeast Portion of the Geysers Geothermal Reservoir. Geothermal GrittoRes. Council, Transactions, 14. In: 2001 Annual Meeting; San Diego, CA. 2001

[19] Bonner B, Hutchings L, Kasameyer P. A strategy for interpretation of microearthquake tomography results in the Salton Sea geothermal field based upon rock physics interpretation of state 2-14 borehole logs. In: Geothermal Resources Council, Transactions, 14, 2006 Annual Meeting; Reno, NV. LLNL, UCRL-PROC-222141. 2006

[20] Zucca JJ, Hutchings LJ, Kasameyer PW. Seismic velocity and attenuation structure of the geysers geothermal field, California. Geothermics. 1994;**23**: 111-126

[21] Menke W. Geophysical Data Analysis: Discrete Inverse Theory. San Diego: Academic Press, an Imprint of Elsevier; 2012

[22] Toksoz MN, Johnston DH, Timur A. Attenuation of seismic waves in dry and saturated rocks: I. Laboratory measurements. Geophysics. 1979;**44**(4): 111-134

[23] Kachanov M, Kachanov B, Tsukrov I. Handbook of Elasticity Solutions. New York: Kluwer Academic Publishers; 2017

[24] Guilham A, Hutchings L, Dreger D, Johnson L. Moment tensor inversions of small earthquakes in the Geysers Geothermal Fields, California. Journal of Geophysical Research. 2014;**119**: 2121-2137

[25] Johnson L. A source model for induced earthquakes at the geysers geothermal reservoir. Pure and Applied Geophysics. 2014;**171**(8):110-142. DOI: 10.1007/s00024-014-0798-7A

[26] Julian BR, Foulger GR. Earthquake mechanisms from linear-programming inversion of seismic-wave amplitude ratios. Bulletin of the Seismological Society of America. 1996;**86**(4):972-980

[27] Johnson L. Source mechanisms of induced earthquakes at the geysers geothermal reservoir. Pure and Applied Geophysics. 2014;**171**(8):1641-1668

[28] Elkibbi M, Yang M, Rial JA. Crack-induced anisotropy models in The Geysers geothermal field. The Northwest Geysers EGS Demonstration Project; California. 2005

[29] Crampin S, Booth DC. Shear-wave splitting showing hydraulic dilation of pre-existing joints in granite. Scientific Drilling. 1989;**1**:21-26

[30] Wu H, Lees JM. Cartesian parameterization of anisotropic traveltime tomography. Geophysical Journal International. 1999;**137**:64-80

[31] Chapman CH, Pratt RG. Traveltime tomography in anistropic media-I. Theory. Geophysical Journal International. 1992;**109**:1-19

[32] Lou M, Rial J. Characterization of geothermal reservoir crack patterns using shear-wave splitting. Geophysics. 1997;**62**:487-494

[33] Boitnott GN, Bonner BP. Characterization of rock for constraining reservoir scale tomography

at the geysers geothermal field. In: Proceedings, Ninteenth Stanford Workshop on Geothermal Reservoir Engineering. 1994

[34] Tarif P, Bourbie T. Experimental comparison between spectral ratio and rise time techniques for attenuation measurement. Geophysical Prospecting. 1987;**35**:668-680

[35] Ingebritsen SE, Manning CE. Permeability of the continental crust: Dynamic variations inferred from seismicity and metamorphism. Geofluids. 2010;**10**:193-205

[36] O'Connell RJ, Budiansky B. Seismic velocities in dry and saturated cracked solids. Journal of Geophysical Research. 1974;**1974**:5412-5426

[37] Boitnott GN. Laboratory measurements on reservoir rocks from the geysers geothermal field. In: Proceedings, Twentieth Workshop on Geothermal Reservoir Engineering, Stanford University, Stanford, California; January 24-26, 1996. SGP-TR-150. 1995

[38] Winkler K, Nur A. Pore fluids and seismic attenuation in rocks. Geophysical Research Letters. 1979; **6**(1):1-4

[39] Gritto R. Chapter 5.0. Towards the Understanding of Induced Seismicity in Enhanced Geothermal Systems, Final Report. Performance Period: January 29, 2010 through May 31, 2014. Sponsored by Golden Field Office, U.S. Department of Energy, Award No. DE-EE0002756. Principal Investigator: Roland Gritto. 2015

[40] Jeanne P, Rutqvist J, Hutchings L, Singh A, Dobson PF, Walters M, et al. Degradation of the mechanical properties imaged by seismic tomography during an EGS creation at The Geysers (California) and geomechanical modeling. Physics of the Earth and Planetary Interiors. 2015;**240**: 82-94

[41] Evans B, Fredrich JT, Wong T-f. The brittle-ductile transition in rocks: Recent experimental and theoretical progress. In: Duba AG, Durham WB, Handin JW, Wang HF, editors. The Brittle-Ductile Transition in Rocks: The Heard Volume. Washington, DC: American Geophysical Union; 1990. pp. 1-20

[42] Kohlstedt DL, Evans B, Mackwell SJ. Strength of the lithosphere: Constraints imposed by laboratory experiments. Journal of Geophysical Research. 1995; **100**:17587-17602

[43] Darot M, Gueguen Y, Baratin M. Permeability of thermally cracked granite. Geophysical Research Letters. 1992;**19**:869-872

[44] Garcia J, Hartline C, Walters M, Wright M, Rutqvist J, Dobson PF, et al. The northwest geysers EGS demonstration project, California part 1: Characterization and reservoir response to injection. Geothermics. 2016;**63**: 97-110

[45] Tokzoz MN, Johnston DH, Timur A. Attenuation of seismic waves in dry and saturated rocks: I. Laboratory measurements. Geophysics. 1979;**44**: 681-690

[46] Johnston DH, Tokzoz MN. Ultrasonic *P* and *S* wave attenuation in dry and saturated rocks under pressure. Journal of Geophysical Research. 1980; **85**:925-936

[47] DeVilbiss-Munoz JW. Wave Dispersion and Absorption in Partially Saturated Rocks [Ph.D. Dissertation]. Stanford University; 1980

[48] Mavkov GM, Nur A. Wave attenuation in partially saturated rocks. Geophysics. 1979;**44**:161-178. DOI: 10.1190/1.1440958

[49] Lowenstern JB, Janik CJ. The Origins of Reservoir Liquids and Vapors from the Geysers Geothermal Field. California (USA): U.S. Geological Survey; 2002 https://volcano.wr.usgs.gov/observatories/yvo/jlowenstern/geysers/Low_Geys.pdf